Article:

Chaurasiya, R., Srivastava, S., Chatterjee, P. et al. (2026) On the relationship between solar spicules and propagating coronal disturbances: the role of shocks. The Astrophysical Journal, 1005 (1). 111. ISSN: 0004-637X

https://doi.org/10.3847/1538-4357/ae75eb

The Astrophysical Journal, 1005:111 (12pp), 2026 July 1 https://doi.org/10.3847/1538-4357/ae75eb

On the Relationship between Solar Spicules and Propagating Coronal Disturbances: The Role of Shocks

Ravi Chaurasiya[1,2,9], Sankalp Srivastava[3,4,9], Piyali Chatterjee[3,4], Sahel Dey[5], Robertus Erdélyi[6,7,8], and Ankala Raja Bayanna[1]
[1] Udaipur Solar Observatory, Physical Research Laboratory, Udaipur-313001, India; ravi@prl.res.in, chaurasiyaravi809@gmail.com
[2] Indian Institute of Technology, Gandhinagar, Gujarat-382355, India
[3] Indian Institute of Astrophysics, 2nd Block, Koramangala, Bengaluru-560034, India
[4] Pondicherry University, R.V.Nagar, Kalapet, Puducherry-605014, India
[5] School of Science, University of Newcastle, University Drive, Callaghan, NSW 2308, Australia
[6] Solar Physics and Space Plasma Research Centre (SP2RC), School of Mathematical and Physical Sciences, University of Sheffield, Sheffield S3 7RH, UK
[7] Department of Astronomy, Eötvös Loránd University, Budapest, Pázmány P. sétány 1/A, H-1117, Hungary
[8] Gyula Bay Zoltán Solar Observatory (GSO), Hungarian Solar Physics Foundation (HSPF), Petőfi tér 3., Gyula H-5700, Hungary
Received 2026 April 21; revised 2026 May 20; accepted 2026 May 29; published 2026 June 29

Abstract

Spicules and propagating coronal disturbances (PCDs) are ubiquitous dynamic features of the solar atmosphere, yet their physical connection remains an open question of paramount importance to the mass and energy transport in the solar atmosphere. Using concurrent multiwavelength high-resolution observations from the Swedish 1 m Solar Telescope and the Solar Dynamics Observatory, supported by two-dimensional radiative magnetohydrodynamic (MHD) simulations, we find that (i) shock waves in the chromosphere generated from nonlinear wave steepening drive some spicules, (ii) in the corona, these shock waves may transition into large amplitude nonlinear compressive MHD waves depending on the magnetic field strength and the ambient coronal conditions. In either case, the shocks or the large-amplitude compressive waves in the corona also transport mass flux upward and produce intensity variations in the form of PCDs in coronal passbands. Further, a multi-height wavelet analysis shows dominant $\sim$5 minute periods in the lower chromosphere that evolve into longer periods ($\geqslant$10 minutes) at higher atmospheric layers, consistent with dispersive propagation in a stratified medium. The observational characteristics, together with the numerical simulations, demonstrate that a shock-driven MHD mechanism links spicule formation to coronal disturbances. Finally, mass flux estimates from both the observations and the simulations indicate that these PCDs can also aid in supplying mass to the solar wind.

Unified Astronomy Thesaurus concepts: Solar spicules (1525); Shocks (2086); Radiative magnetohydrodynamics (2009); Magnetohydrodynamical simulations (1966); Solar chromosphere (1479); Solar atmosphere (1477); Solar physics (1476)

Materials only available in the online version of record: animation

1. Introduction

The solar atmosphere is a highly dynamic environment where magnetic fields and plasma flows interact in complex ways, giving rise to a variety of fine-scale structures. Among these spicules, which are thin jet-like features observed prominently at the solar limb (J. M. Beckers 1972; G. Tsiropoula et al. 2012) and on the solar disk as mottles or dynamic fibrils (G. Tsiropoula et al. 1994; Y. Suematsu et al. 1995; V. H. Hansteen et al. 2006), are of particular interest due to their ubiquity and their potential role in mass and energy transport into the solar corona (M. Carlsson et al. 2019; L. Ni et al. 2026). Spicules exhibit rapid upward and downward motions and, in many cases, are heated to transition region (TR) and coronal temperatures (T. M. D. Pereira et al. 2014; L. Rouppe van der Voort et al. 2015; R. Chaurasiya et al. 2024; S. Bose et al. 2025).

[9] Both authors contributed equally to this work.

Although significant progress has been made in understanding the heating of spicular plasma to such high temperatures, the precise physical mechanisms responsible for their formation and dynamics remain a subject of debate (M. Carlsson et al. 2019). Several mechanisms have been proposed to explain the origin and driving of these spicules. These include shock waves generated by the leakage of photospheric oscillations into the chromosphere (B. De Pontieu et al. 2004; V. H. Hansteen et al. 2006; L. Heggland et al. 2011; T. Gopalan Priya et al. 2018; S. Dey et al. 2022). A recent study by S. Srivastava et al. (2025) found that the strength of the shock is well correlated with the height of the corresponding spicule in their two-dimensional radiative magnetohydrodynamic (rMHD) simulations. Alternative drivers of spicules could be Alfvén waves or pulses (H. Iijima & T. Yokoyama 2017; W. Oxley et al. 2020; T. Sakaue & K. Shibata 2020; A. K. Srivastava et al. 2024), and magnetic reconnection in small-scale magnetic configurations (J. Y. Ding et al. 2011; V. Yurchyshyn et al. 2013; T. Samanta et al. 2019; J. J. González-Avilés et al. 2020). Other processes such as granular buffeting (B. Roberts 1979), rebound shocks (J. V. Hollweg 1982; K. Murawski & T. V. Zaqarashvili 2010), chromospheric swirls (J. Liu et al. 2019), the release of amplified magnetic tension facilitated by ambipolar diffusion (J. Martínez-Sykora et al. 2017), and Ellerman bombs

(M. O. Sand et al. 2025) have also been suggested as possible drivers. Although each mechanism provides valuable insight, it is more likely that multiple processes operate simultaneously or under different solar conditions, giving rise to the dynamic nature of the spicules.

In addition to their importance in chromospheric and TR dynamics, spicules are also believed to play a role in shaping disturbances in the solar corona. Observations have revealed upward-propagating disturbances in coronal structures, appearing as intensity perturbations, that have also been linked to spicular activity (e.g., F. Jiao et al. 2015; S. J. Skirvin et al. 2024). There is an indication that both waves and flows might be responsible for the origin of these propagating coronal disturbances (PCDs); however, the debate has not yet been fully settled (e.g., P. Bryans et al. 2016; J. Martínez-Sykora et al. 2018; D. Banerjee et al. 2021). Since the lower solar atmosphere is replete with shock waves, it can be expected that they possibly serve an important role in linking spicules and PCDs. Furthermore, recent quiet-Sun chromospheric modeling has suggested that a conversion of chromospheric acoustic shocks back into linear waves might introduce considerable slow MHD wave flux into the corona (Q. Noraz et al. 2026). However, a comprehensive physical picture linking the spicules and spicule-driving shocks seen in the lower atmosphere to the PCDs is still missing, which can be crucial for understanding whether spicules play a role in supplying energy and mass to heat the solar corona and drive the solar wind (G. L. Withbroe & R. W. Noyes 1977), the primary agent of space weather.

In this work, we focus on studying the spicules driven by shock waves and their role in triggering PCDs. We investigate this connection among spicules, shocks, and PCDs through high-resolution multiwavelength observations and further support our findings with insights from two-dimensional radiative MHD simulations. We also present mass flux estimates from both observations and simulations and show how they relate to the mass-loss rate of the solar wind.

2. Association of Shock-driven Spicules with PCDs: Observational Signatures

We analyzed a coordinated dataset of NOAA Active Region 12760, observed on 2020 April 30 from 07:58 to 09:37 UT using the Swedish 1 m Solar Telescope (SST; G. B. Scharmer et al. 2003) and the Solar Dynamics Observatory (SDO; W. D. Pesnell et al. 2012). The heliocentric coordinates of the target region were approximately (374″, −70″), corresponding to an observing angle of $\mu = 0.92$. The active region contained multiple solar pores and network structures with a moderate magnetic field strength (see Figure 1). The field of view of the observations is approximately 60″ × 60″. Further details of the SST and SDO observations, including spectral sampling, cadence, alignment procedures, and the inversion, are provided in Appendix A.

Motivated by earlier studies identifying sawtooth patterns in λ–t diagrams as a characteristic observational signature of shock waves in the lower solar atmosphere (M. Carlsson & R. F. Stein 1997; L. H. M. Rouppe van der Voort et al. 2003; R. Chaurasiya et al. 2025), we explore the role of shock waves in driving spicules and examine their relation with PCDs within the region under study.

First, we manually inspected the λ–t diagrams at the footpoints of spicules to investigate whether the spicules originate from locations associated with chromospheric shock waves. Figure 2

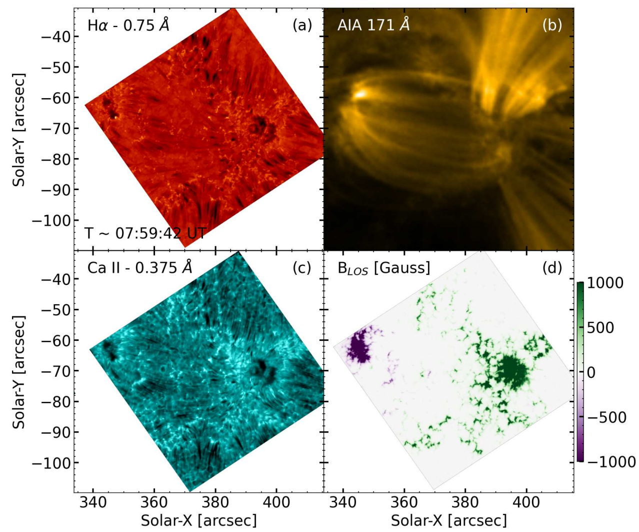

Figure 1. Panels (a) and (c) show the chromosphere of the active region as observed in the blue wings of Hα (Hα −0.8 Å) and Ca II IR (Ca II IR −0.375 Å), respectively. Panels (b) and (d) display the lower corona as observed in AIA 171 Å and the photospheric magnetic field inferred from `PyMilne` inversion (J. de la Cruz Rodríguez 2019) of Fe I 6173 Å, respectively. The spicules may be identified as elongated absorption features appearing as dark threads over panels (a) and (c).

shows concurrent observations of the low chromosphere and the low corona in the Hα −0.75 Å wing and the AIA 171 Å channel, together with the λ–t diagrams in Hα and Ca II 8542 Å corresponding to the base of the slit (marked by the magenta X). From panel (a), it is evident that the footpoint of a spicule spatially coincides with a location exhibiting shock wave signatures, characterized by episodic sawtooth patterns in time. It appears that the characteristic sawtooth patterns are more prominent in the Ca II 8542 Å data primarily because the Ca II 8542 Å line has a narrower core compared to the broader Hα line core, making shock signatures easier to detect. In addition, the Ca II 8542 Å observations have a finer spectral sampling (∼7.5 mÅ) compared to the Hα observations (∼25 mÅ). The combined effect of the broader line core and coarser spectral sampling in Hα reduces the ability to resolve rapid spectral variations associated with shock propagation. As a result, the shock wave signatures (characteristic sawtooth patterns) appear much clearer in the Ca II 8542 Å λ–t diagrams than in the Hα data. These sawtooth patterns indicate strong chromospheric upflows followed by subsequent downflows.

To further investigate the possible connection between shock-driven spicules in the chromosphere and PCDs in the corona, we constructed space–time (x–t) maps by placing a virtual slit of width 7 pixels (corresponding to approximately 0.3 Mm) across the chromosphere and the corresponding SDO/Atmospheric Imaging Assembly (AIA) channels, as shown in Figure 3. The resulting x–t maps of the Hα line core and wing clearly illustrate that spicules trace parabolic trajectories as part of their evolution. The projected initial velocities of the spicules range between ∼7.91 and ∼15.98 km s^{-1}. The signatures of PCDs in the corona are identified in the x–t diagrams of multiple AIA filters, revealing a temporal coincidence between the onset of the PCDs and shock-driven spicules. This correspondence indicates that shock-driven spicular activity plays a pivotal role in triggering PCDs. It is also evident that PCDs follow approximately a linear characteristic curve in x–t maps, which

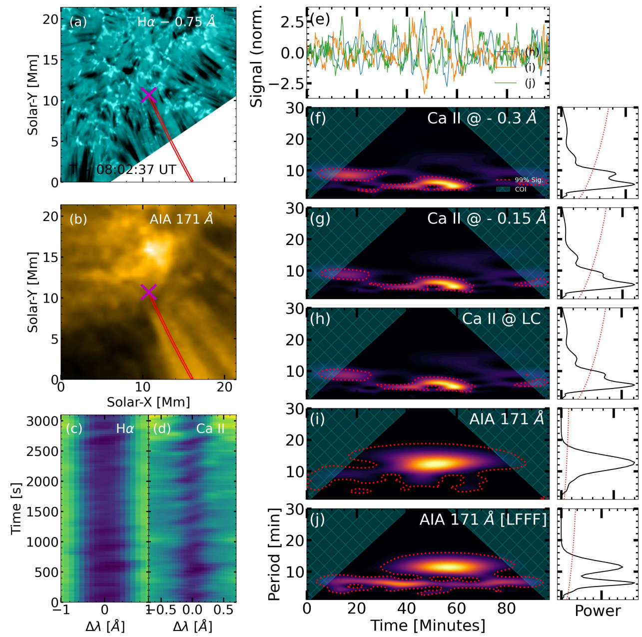

Figure 2. Panels (a) and (b) show the chromospheric and the low coronal structures of the solar atmosphere as observed in the blue wing of Hα and AIA 171 Å, respectively. Panels (c) and (d) present the λ–t diagrams of the Hα and Ca II 8542 Å spectral lines at the location marked by the cross (X) in panel (a). The red slit (or box) in panels (a) and (b) indicates the region used to construct the x–t map shown in Figure 3. Panel (e) shows the time series of the normalized Doppler signals of the Ca II 8542 Å line center and AIA 171 Å light curves only for clarity. Panels (f)–(h) display the wavelet analysis of the Ca II 8542 Å Doppler velocity time series (indicated in panel (e)), obtained at multiple heights at the shock wave locations covering lower to upper chromosphere, whereas panel (i) presents the wavelet analysis of the corresponding AIA 171 Å light curve (shown in panel (e)). Panel (j) also presents the wavelet analysis of the AIA 171 Å light curve, but for the location obtained from the LFFF extrapolation, as indicated by the red magnetic field line in Figure 13.

refers to constant projected propagation speed between ∼37.95 and ∼44.98 km s^{-1} for different events. Two additional examples similar to those in Figure 2 are presented in Figures 9 and 10, with their corresponding space–time maps shown in Figures 11 and 12, respectively.

The wavelet analysis of the multi-height Doppler velocities sampling different atmospheric layers in the chromosphere (panels (e)–(g)) and the AIA 171 Å intensity signal sampling the lower corona (panel (h), assuming vertical propagation), for this shock event, is also presented in Figure 2. The details of the estimation of the multi-height Doppler velocities are provided in Appendix B. However, since coronal magnetic field lines are generally inclined rather than strictly vertical, we additionally performed wavelet analysis of the AIA 171 Å signal along the magnetic field-aligned trajectory obtained from linear force-free field (LFFF; see Appendix E for details) extrapolation, as shown in panel (j). The extrapolated magnetic field geometry is illustrated in Figure 13. Notably, the wavelet power distribution changes slightly when the signal is sampled along the inclined magnetic field line compared to the vertically projected location above the chromospheric pixels shown in panels (i).

3. Insights from the Radiative MHD Simulations

The relationship among the spicules, shocks, and PCDs is further explored utilizing a fully compressible radiative MHD model, which considers multiple magnetic network regions. The simulation setup (in The `Pencil Code`[10]) is a 2D Cartesian box covering a vertical range from 5 Mm below the photosphere to 31 Mm above. The vertical extent includes the upper convection zone, photosphere, chromosphere, TR, and lower corona. The horizontal extent of the domain is 18 Mm, which captures several convective granulation cells. The uniform grid spacing is 24 km in both the horizontal and vertical directions. The model incorporates the essential physics needed to comprehensively model the highly stratified solar atmosphere, including Spitzer thermal conduction, an ionized equation of state (with ionization fraction calculated using the Saha ionization formula), solving the detailed LTE radiative transfer equation for the optically thick regime, and tabulated radiative cooling in the optically thin upper atmosphere.

The overall magnetic field resembles an open field topology, with an imposed vertical background field $B_{\rm imp}$. We analyze two different models with $B_{\rm imp} = 10$ G and $B_{\rm imp} = 50$ G while keeping all other parameters the same, and compare the results. The horizontal boundaries are periodic, while the top boundary is maintained at a constant temperature of 1 MK. A sponge layer in the uppermost 6 Mm of the domain is included to absorb any reflection of the outgoing waves from the top boundary. No additional magnetic flux emergence is employed in the domain. Further details regarding the model can be found in S. Dey et al. (2022), K. Kesri et al. (2024), and S. Srivastava et al. (2025). An example of the relaxed temperature and density structuring in the simulation setup for the $B_{\rm imp} = 10$ G case is shown in Figure 4, after the convection has saturated. The snapshot corresponds to the first snapshot of the analyzed time series. The model is able to self-consistently excite a forest of spicules as a result of the subsurface convective processes, as shown in Figure 5. We analyzed a 60 minute long time series of snapshots from the simulations, taken at a cadence of 20 s, to study the link between the spicules and shocks and how this relationship manifests itself in the corona when observed through EUV synthetic emission. In Figures 5(a) and (d), spicules are seen as enhanced fine-scale emission structures at 15,000 K for 10 and 50 G imposed magnetic fields, respectively. The slow shock wave fronts, which propagate along the local magnetic field, are identified in the simulation domain using the automated shock detection technique (discussed in Appendix F) and marked with magenta points (panels (b) and (e) of Figure 5). The leakage of global solar oscillations at the photosphere cascades into the highly stratified atmosphere above and steepens to shock waves. In our model, spicular jets are primarily driven and accelerated by these nonlinear shock waves that are found to be located at the spicule tips during the spicule rise phase. These localized fronts are associated with strong flow convergence regions, as shown in panels (b) and (e) of Figure 5 for 10 and 50 G imposed magnetic fields, respectively. However, not all converging flow regions correspond to shock waves. By definition, at a slow shock front, the flow speed in the rest frame of the shock must jump from *superslow* (greater than slow MHD speed) to *subslow* (less than slow MHD speed) while moving from the upstream to the downstream region.

For understanding the impact of the spicules and/or propagating shock waves in the corona, we investigate a

[10] https://pencil-code.org/

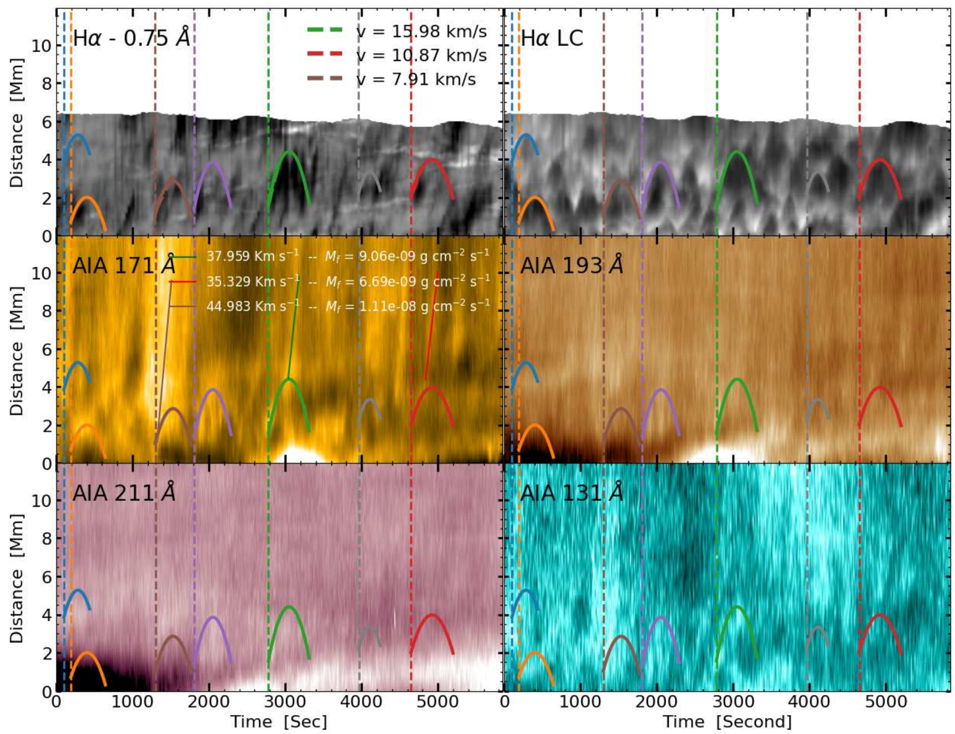

Figure 3. Space–time maps obtained from the virtual slit (see Figure 2) corresponding to the Hα wing, Hα line center, and various SDO/AIA channels. The colored parabolas trace the parabolic trajectories of different spicules. The dashed line on the left side of each parabola is used to estimate the projected velocity. The vertical dashed colored lines mark the onset of shock-driven spicular activity or the beginning of PCDs, indicating that the PCDs are triggered by the shock-driven spicules.

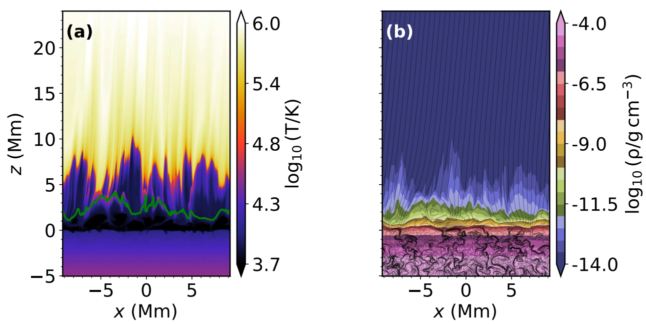

Figure 4. (a) Temperature and (b) density distribution at t = 83.3 minutes from the start of the simulation with an imposed vertical magnetic field $B_{\rm imp}$= 10.0 G. The plasma-β = 1 surface is overplotted with the green line in (a), while the magnetic field lines are overplotted in black in (b).

simultaneous plasma emission map, similar to the coronal temperature-sensitive AIA 171 Å channel (panels (c) and (f) of Figure 5). The coronal emission reveals the highly structured nature of the atmosphere in the presence of spicules and shock structures for both setups. Some of the enhanced emission features are possibly connected to PCDs and are detected much higher in the corona for the 10 G case.

To further determine whether these enhanced emission features originate in situ in the corona or are imprints of chromospheric structures, e.g., the spicule-driving shocks, we utilize time- distance diagrams along a vertical slit of 5 grid point width ($\sim$ 0.12 Mm), for both runs (panels (c) and (g) of Figure 6). They reveal the 15,000 K emission profile wherein spicules trace a parabolic trajectory in time, with the detected slow shocks plotted in magenta. The shocks are seen to move in unison with the spicules during their rise phase, demonstrating their role in driving the spicules. It is noteworthy that our shock-driven spicule picture is distinct from another existing description where the hot tip of spicules induces shocks in the corona (S. Sow Mondal et al. 2022). Furthermore, the strong flow convergence or compression regions, identified in the simulation by setting a threshold on the velocity convergence (see Appendix F), are overplotted in blue. We note that in both 10 and 50 G setups, as we move to greater heights, relatively fewer of the strong convergence or compression regions are detected as slow shocks, since they do not exhibit a jump of the flow velocity from superslow to subslow.

However, many of the compression fronts appear to be continuations of the upward-propagating shock waves after they get separated from the spicules and move into the corona. In other words, often these shock waves (magenta contours) propagating higher up in the atmosphere transform to large-amplitude nonlinear compressive waves (marked in blue isocontours). We also find that for the 50 G imposed magnetic field, shock fronts transition to nonlinear compressive waves at relatively lower heights than for the 10 G run (panel (g) compared to panel (c) of Figure 6), likely due to the suppression of convective power in the presence of a stronger magnetic field. The Mach numbers calculated for the upstream perpendicular flow at a typical compression front around z = 9.2 Mm are 1.1 and 0.4 for the 10 and 50 G cases, respectively (in the rest frame of the front). The asymmetric or nonlinear nature of the waves is confirmed by examining the time variation of vertical velocity extracted at different heights along the slit, as indicated by the red dashed lines in panels (c) and (g) of Figure 6. The vertical velocity profiles, depicted in panels (a) and (e) of Figure 6, show steepening into a sawtooth or an N-shaped profile as we go up in the atmosphere, signaling the development of a nonlinear wave. Notably, the sawtooth profile is present at the lower heights where spicules

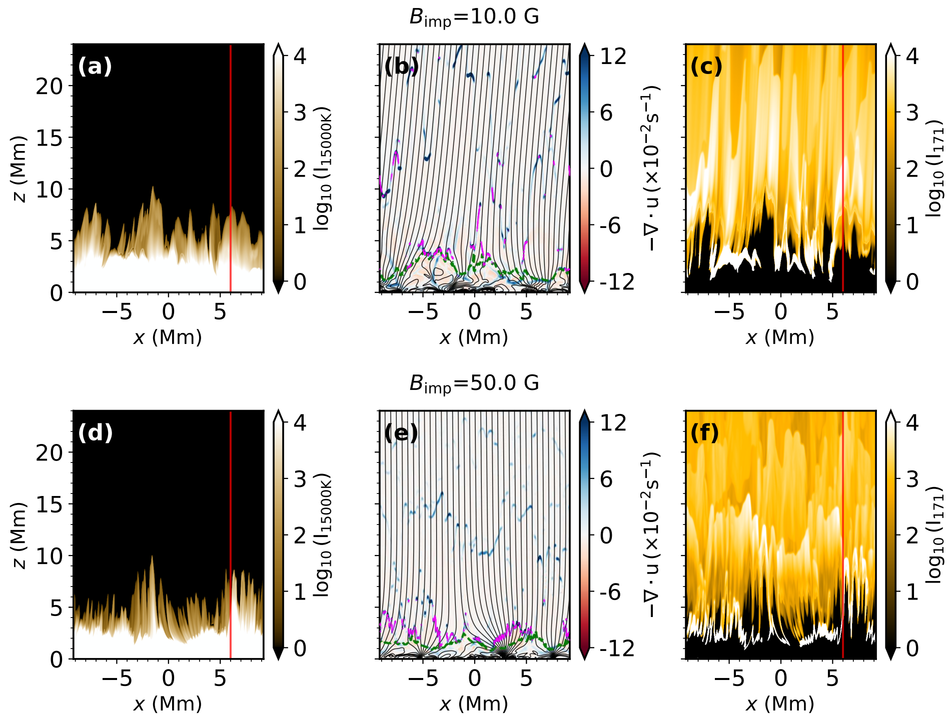

Figure 5. Panels (a)–(c) show a snapshot at a time of $t = 83.3$ minutes from the start of the simulation with an imposed vertical magnetic field B_{imp}= 10.0 G. The spicules are visible in the synthetic emission at 15,000 K in (a), while the associated PCDs can be seen in the synthetic AIA 171 Å emission in (c). The slit used for obtaining the time–distance diagrams in Figure 6 is depicted by red lines in both (a) and (c). Panel (b) depicts the velocity convergence regions (blue). Additionally, the strong convergence regions that qualify as slow shocks are overplotted in magenta. The plasma-$\beta = 1$ contour is shown as a green dotted line. Panels (d)–(f) are similar to (a)–(c) but for $B_{imp} = 50.0$ G at $t = 83.3$ minutes from the start of the simulation. (An animation of this figure for 60 minutes of solar time is available in the online article.)

(An animation of this figure is available in the online article.)

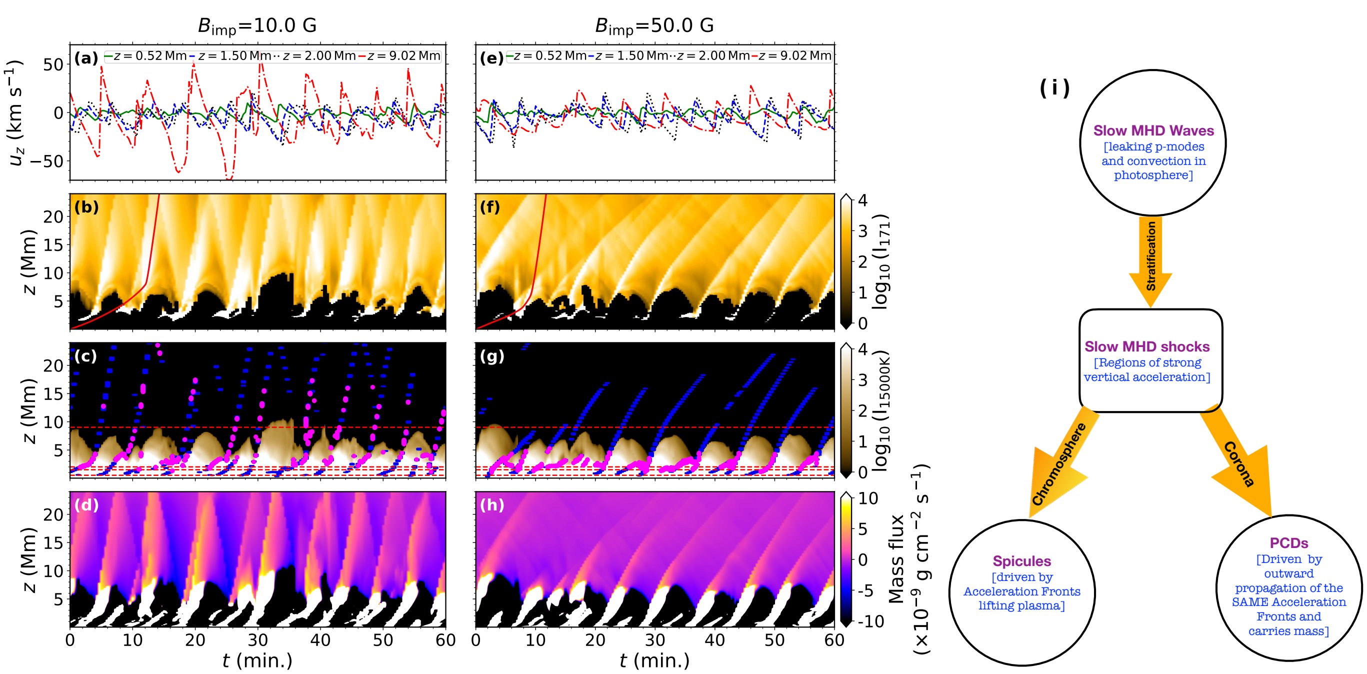

Figure 6. (a) Time variation of vertical velocity extracted at different heights (see the legend) along the vertical slit (of width 5 grid spacings) placed at $\sim x = 6.0$ Mm (depicted in Figure 5(a)) for the simulation with $B_{imp} = 10.0$ G. (b)–(d) Time–distance plots along the same vertical slit. The synthetic emission for the AIA 171 Å channel in panel (b) shows the coronal intensity enhancements or PCDs, propagating upward, with the red solid line depicting the sound speed characteristic curve along the slit. In panel (c), we show the 15,000 K synthetic emission, in which the spicules trace a parabolic trajectory in time. The strong flow convergence or compression regions are overplotted in blue, out of which only the detected slow shocks are indicated in magenta. The red horizontal dashed lines show the heights where the vertical velocity time series in (a) have been extracted. Panel (d) depicts the vertical mass flux along the same vertical slit. Panels (e)–(h) are similar to (a)–(d), but for the second simulation with $B_{imp} = 50.0$ G. (i) A schematic to show the causality of shock, spicule, and PCD connection as deduced from simulations.

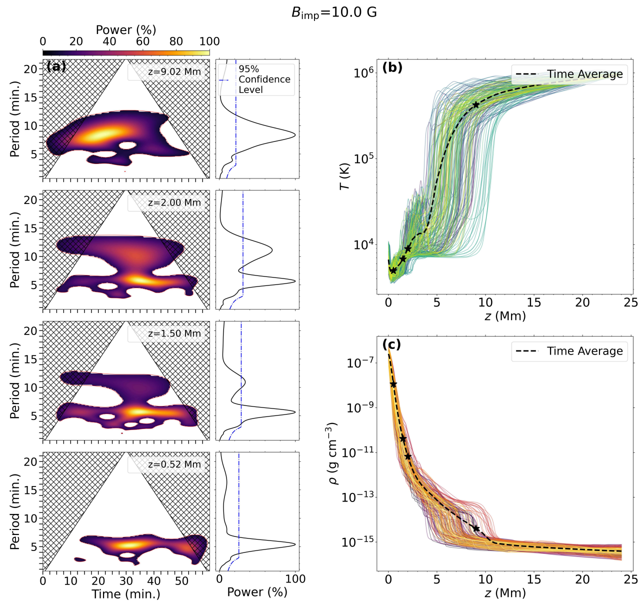

Figure 7. (a) The wavelet analysis of the vertical velocity time series sampled at multiple heights in the $B_{\rm imp} = 10$ G simulation run of Figure 6(a). The left panels show the wavelet power above the 95% significance level (with areas outside the cone of influence marked using a hatched pattern), while the corresponding line plots to the right show the global wavelet power spectrum. The blue dotted–dashed curves in the right panels show the 95% confidence level. (b), (c) Temperature and density stratification profiles, respectively, along the vertical slit of 5 grid points width around $x = 6.0$ Mm, for the run: colored lines correspond to the stratification at different times in the 60 minute duration of the synthetic data. The black dashed line shows the time-averaged variation of temperature or density as a function of z. In order to assess the effect of the steep stratification on the dominant period, the asterisk (black) symbols mark the heights above the photosphere at which the wavelet analysis is performed.

(and slow shocks) can be detected, consistent with our observational findings (Figure 2). At upper atmospheric heights, the asymmetric or nonlinear shape is retained, even though it is not a shock anymore, since it does not show a jump in flow velocity from superslow to subslow across it. Furthermore, we notice that the magnitude of the vertical velocity is less for the 50 G case than for the 10 G one, again indicative of weaker convective power for the higher magnetic field. In the time–distance plots (panels (b) and (f) of Figure 6) of AIA 171 Å synthetic emission, we can notice the good correspondence (in terms of the slope) of the coronal intensity enhancements or PCDs (propagating upward) with these compression fronts (associated with strong positive vertical acceleration in our model). The typical characteristic speeds of PCDs are determined from the slopes of the time–distance plots, which are 95.8 and 26.5 km s^{-1} at $z = 15$ Mm for the 10 and 50 G imposed fields, respectively. The sound speed characteristic curve is denoted (in red) for comparison with the PCD propagation speed for both the $B_{\rm imp}$ cases. For the higher $B_{\rm imp}$, we find that the propagation speed of the synthetic PCDs falls well below the sound speed in the corona.

The compression fronts in corona, as discussed, are the imprints of spicule-driving slow shocks in the lower atmosphere. Further, the schematic in panel (i) of Figure 6 presents a unified picture from our model in which slow MHD waves generated by photospheric convection steepen into shocks, lifting chromospheric plasma to form spicules while the same acceleration fronts propagate upward, giving rise to PCDs. As these fronts move into the corona, they might transition into nonlinear MHD waves depending on the ambient magnetic field strength and coronal temperature, linking spicules and PCDs as different manifestations of the same shock-driven dynamics across atmospheric layers.

Moreover, these nonlinear waves are capable of carrying mass flux outward into the corona, as shown in panels (d) and (h) of Figure 6, depicting time–distance plots of vertical mass flux along the same vertical slit of Figure 5(a).

The corresponding wavelet analysis of the multi-height vertical velocity profiles for the 10 G run (panel (a) of Figure 6) is shown in Figure 7(a) for different heights. We find the peak or the dominant period of the velocity signal is at ∼5 minutes for lower atmospheric heights ($z = 0.5$ Mm). The 5 minute period corresponds to the leakage of global solar acoustic oscillations in the lower atmosphere. In the chromospheric region ($z = 1.5$–2.0 Mm), a secondary peak, corresponding to ∼10 minutes of periodicity, emerges along with the primary 5 minute mode. However, the dominant power completely shifts to ∼10 minutes of periodicity at the coronal heights (for example, $z = 9$ Mm). This transition from lower to higher dominant period, as we move from low chromosphere to corona, is similar to the observed signals, where the peak power is detected at ∼13 minutes for the AIA 171 Å channel (highlighted in Figure 2). The increase in dominant period behavior might be described in terms of dispersive propagation of waves in a highly stratified medium, as shown in panels (b) and (c) of Figure 7 for temperature and density stratification profiles, respectively. Overall, the 50 G run also shows a similar nature of shift in the dominant period with increasing height in the atmosphere.

4. Discussion and Conclusions

In this work, we investigated the origin of a subset of chromospheric spicules that appear to be driven by shock waves using concurrent high-resolution observations together with two-dimensional rMHD simulations. The observations identify these events through characteristic sawtooth patterns in λ–t diagrams at the spicule footpoints, a well-known signature of shock formation produced by the nonlinear steepening of upward-propagating waves in a stratified atmosphere. The key observational result is that the spicules originate from locations exhibiting these chromospheric shock signatures and are followed by upward-propagating intensity disturbances detected in coronal passbands (Figures 2, 3, and 9–12), suggesting that the chromospheric shocks responsible for the launch of the spicules may also generate the coronal disturbances observed above them. It is noteworthy that these shock locations do not show any clear magnetic flux cancellation in the photosphere, as indicated by the magnetograms derived from the PyMilne inversion of the SST Fe I 6173 Å photospheric line. While the spicules exhibit an average projected velocity of ∼11 km s^{-1} in the chromosphere, as inferred from the Hα −0.75 Å filtergrams, the associated PCDs display significantly higher projected velocities of ∼40 km s^{-1} in the overlying corona.

While these observations reveal a clear temporal and spatial association, the radiative MHD simulations provide the physical framework needed to interpret these observations. In the simulations, slow MHD waves generated by photospheric convection steepen into shocks as they propagate upward through the stratified atmosphere. These shocks accelerate chromospheric plasma upward, producing spicular jets whose tips coincide with the locations of the detected slow shocks. As the same acceleration fronts continue to propagate into the corona, they generate compressive disturbances that appear as intensity enhancements in synthetic EUV emission maps. This demonstrates that the same upward-propagating shock fronts that drive the spicules can continue into the corona, and naturally produce PCD-like disturbances. L. Ni et al. (2026) have also reported compressive structures associated with spicule upflows and interpret them as slow-mode shocks present at both chromospheric and coronal heights. However, the temporal evolution required to distinguish between upward-propagating shocks and in situ formation is not explicitly demonstrated. In contrast, our analysis tracks the evolution of disturbances across multiple atmospheric layers, showing that the same upward-propagating shock fronts naturally account for both spicule formation and the associated coronal disturbances.

The simulations capture several key properties inferred from the observations. The shock fronts are bands of strong vertical pressure acceleration, which coincide with the tips of the spicules during their rise. These upward-propagating shocks or compressive fronts impart impulsive acceleration to plasma parcels as they pass. The successively affected plasma parcels evolve ballistically under gravity and magnetic forces, appearing as spicules in chromospheric and TR channels. The same compressive fronts frequently evolve into large-amplitude nonlinear compressive waves as they progress into the corona in the form of propagating disturbances. Whether these disturbances remain true slow shocks or transition into nonlinear MHD waves depends on the magnetic field strength and the ambient coronal conditions. In either case, the disturbances continue to propagate upward, producing density and temperature perturbations that manifest as intensity variations in coronal channels.

The simulations also support the observed trend in dominant oscillation period with atmospheric height. The chromospheric signal is dominated by periods of approximately 5 minutes, consistent with the leakage of photospheric *p*-mode oscillations and MHD wave propagation in magnetic flux tubes. At coronal heights, the dominant period increases to approximately 10 minutes or longer. In the simulations, this shift arises naturally as waves propagate through the strongly stratified atmosphere where density decreases rapidly, and temperature increases sharply. Under these conditions, different frequency components propagate at different speeds, producing a dispersive evolution of the wave packet. In addition, shocks generated at slightly different times in the lower atmosphere can merge during upward propagation (J. Chae et al. 2015), producing longer-period disturbances at higher altitudes.

Because slow MHD waves propagate primarily along magnetic field lines, the coronal response is not necessarily located directly above the chromospheric shock location. The coronal magnetic field is typically inclined, implying that measurements of coronal emission must be taken along the corresponding magnetic field-aligned trajectory rather than at the vertically projected pixel. This effect is illustrated in panels (i)–(j) of Figure 2, where the wavelet power differs when the AIA signal is sampled along the extrapolated magnetic field line compared to the vertically projected location, and in the three-dimensional magnetic field configuration shown in Figure 13. In such cases, magnetic field extrapolation techniques, such as LFFF or related methods, provide a more physically consistent way to trace the field-aligned propagation path and identify the appropriate coronal sampling location.

Another important result concerns the mass flux associated with these disturbances. At heights above ∼15 Mm, the horizontally averaged mass flux in the simulation becomes approximately constant with height, indicating that most of the returning chromospheric plasma has already fallen back. The resulting net upward mass flux, averaged over five cycles, is $\langle \rho u_z \rangle_t \sim (1.1–3.5) \times 10^{-11}\,\mathrm{g\,cm^{-2}\,s^{-1}}$. The mass flux is less for the 50 G case than for the 10 G case. To compare the Cartesian simulation with solar wind observations in spherical geometry, instead of mass flux, we use the conserved quantity of mass-loss rate per unit solid angle, namely, $\langle \rho u_z \rangle r^2$, for a radial outflow at $r = R_\odot$. This value corresponds to $(6 \times 10^{10}–2 \times 10^{11})\,\mathrm{g\,s^{-1}\,sr^{-1}}$, which is comparable to the canonical solar wind value of $\dot{M}_{\rm WN} \sim 7 \times 10^{10}\,\mathrm{g\,s^{-1}\,sr^{-1}}$, estimated from proton density ($\sim 6\,\mathrm{cm^{-3}}$) and wind velocity ($\sim 650\,\mathrm{km\,s^{-1}}$) measured at Earth (G. L. Withbroe & R. W. Noyes 1977). For comparison, the mass flux estimated from both the observed and simulated PCD slopes in $t - z$ images (in Figures 3 and 6) with density inferred from emission measure is $\sim 9 \times 10^{-9}\,\mathrm{g\,cm^{-2}\,s^{-1}}$ and corresponds to a mass-loss rate per solid angle of $\sim 5 \times 10^{13}\,\mathrm{g\,s^{-1}\,sr^{-1}}$. This is more than 2 orders of magnitude larger than the $\dot{M}_{\rm WN}$ value, indicating that this calculation represents a local estimate at an outflow region that does not account for return flows or temporal intermittency. Our simulations show that the PCD slope-based calculation systematically overestimates the net mass flux, but once the physically relevant averaged quantity is considered, it agrees remarkably well with the solar wind mass-loss rate of $\dot{M}_{\rm WN}$. Here, we show that the same upward-propagating acceleration fronts responsible for spicule formation can transport plasma into the corona and generate comparable levels of mass flux. This agreement supports the interpretation that the disturbances observed in coronal channels represent a combination of compressive waves and mass motions driven by the same shock dynamics that produce the spicules.

The main advances of this work compared to previous studies can be summarized as follows:

1. By combining high-resolution SST Hα observations with SDO/AIA coronal imaging, this study traces the evolution of shock-driven dynamics from the low chromosphere to the corona. Unlike earlier studies relying mainly on IRIS and AIA observations, which primarily probe the upper chromosphere and TR, our analysis provides direct evidence linking chromospheric shock-driven spicules with coronal disturbances.
2. We clarify the physical nature of PCDs associated with shock-driven spicules. The simulations show that spicule-driving slow shocks can transition into large-amplitude compressive waves in the corona, producing intensity disturbances that carry both wave energy and mass flux into the upper atmosphere. For this purpose, we rely on the use of an advanced shock detection technique in order to properly assess the role of shocks in the simulations.

Taken together, the observations and simulations support a unified scenario in which chromospheric shocks generated by convective motions and *p*-mode leakage steepen as they propagate upward, drive spicular jets, and continue into the corona as large-amplitude compressive disturbances. These disturbances appear observationally as PCDs and can transport both mass and energy into the upper solar atmosphere. In this framework, spicules and PCDs represent different manifestations of the same underlying shock-driven dynamics operating across multiple atmospheric layers.

Future work incorporating larger statistical samples covering different regions of magnetic geometry, high-resolution three-dimensional simulations, and spectroscopic diagnostics at coronal temperatures will be essential to further quantify the energy flux carried by these disturbances and to evaluate their role in coronal heating and solar wind acceleration. It also remains to be investigated whether other classes of spicules, beyond shock-driven events, exhibit a similar connection with propagating disturbances in the corona.

Acknowledgments

We thank the referee for careful reading of our paper and providing comments that have considerably improved the quality of the presentation. The Swedish 1 m Solar Telescope is operated on the island of La Palma by the Institute for Solar Physics of Stockholm University in the Spanish Observatorio del Roque de los Muchachos of the Instituto de Astrofísica de Canarias. The Swedish 1 m Solar Telescope, SST, is co-funded by the Swedish Research Council as a national research infrastructure (registration No. 4.3-2021-00169). We would like to thank the SST team for making the data publicly available. SDO is a mission for the NASA Living With a Star program. The SDO/Helioseismic and Magnetic Imager (HMI) data were provided by the Joint Science Operation Centre (JSOC). Further, this work used the DiRAC Data Intensive service (DIaL2) at the University of Leicester and CSD3 at the University of Cambridge (project ID: dp261). The DiRAC service at Leicester and Cambridge was funded by BEIS, UKRI, and STFC capital funding and STFC operations grants. DiRAC is part of the UKRI Digital Research Infrastructure. P. C. acknowledges the allocation of computing resources (project ID NAISS 2025/3-69: Astrophysical turbulence and dynamo action) at the PDC Center for High Performance Computing at KTH in Stockholm, funded by the National Academic Infrastructure for Supercomputing in Sweden. The Leo HPC at the Indian Institute of Astrophysics, Bangalore, has also been used to perform the numerical simulation and analysis. S.D. gratefully acknowledges the support provided by the Australian Research Council (ARC) Discovery Project (DP210100709). R.E. acknowledges the NKFIH OTKA (Hungary, grant No. K142987), the Science and Technology Facilities Council (STFC; UK, grant No. ST/M000826/1), the PIFI (China, grant No. 2024PVA0043), and the NKFIH (Hungary) Excellence Grant (grant No. TKP2021-NKTA-64) for enabling this research. This work was also supported by the International Space Science Institute project (ISSI-BJ ID 24-604) on "Small-scale eruptions in the Sun."

Software: The `Pencil Code` (The Pencil Code Collaboration et al. 2021), `NumPy` (C. R. Harris et al. 2020), SciPy (P. Virtanen et al. 2020), `Matplotlib` (J. D. Hunter 2007), `SunPy` (The SunPy Community et al. 2020), `WaLSAtools` (S. Jafarzadeh et al. 2025).

Appendix A
Observational Details

A.1. SST

The SST dataset comprises imaging spectroscopic observations of the Fe I 6173 Å, Hα, and Ca II 8542 Å spectral lines obtained using the CRisp Imaging SpectroPolarimeter (CRISP; G. B. Scharmer et al. 2008), sampling the photosphere and chromosphere, respectively. The temporal cadence of the three spectral lines was approximately 29.23 s, with a spatial sampling of $0''.0591$ pixel^{-1}. The spectral scans consisted of 15, 15, and 17 wavelength positions, respectively, covering ranges of ±0.275, ±1.75, and ±0.7 Å. These observations were processed using the SSTRED reduction pipeline (M. G. Löfdahl et al. 2021). This pipeline employs the multi-object multi-frame blind deconvolution technique (M. Van Noort et al. 2005) to mitigate the effects of atmospheric seeing and instrumental distortions. By combining numerous short-exposure frames, the method reconstructs images with enhanced spatial resolution and improved image quality. The data reduction sequence further includes dark current removal, flat-field calibration, and accurate co-alignment of the reconstructed frames. These procedures produce calibrated and science-ready CRISP datasets suitable for detailed analysis (J. de la Cruz Rodríguez et al. 2015).

To infer the photospheric magnetic field, `PyMilne` (J. de la Cruz Rodríguez 2019) inversion code has been applied to the Fe I 6173 Å observation. Datasets were co-aligned by cross-correlating nearly simultaneous wing images dominated by photospheric features. The SST dataset is publicly available through the SST archive.[11]

A.2. SDO

The registered cutouts were obtained using the SDO cutout service, which provides EUV data from the AIA (J. R. Lemen et al. 2012) and continuum images and magnetograms from the HMI (P. H. Scherrer et al. 2012). The AIA UV channels (1600, 1700 Å) and EUV channels (94–335 Å) have nearly identical plate scales of $0''.6$ pixel^{-1}, but cadences of 24 s (UV) and 12 s (EUV). HMI line-of-sight magnetograms and continuum images have a plate scale of $0''.5$ pixel^{-1} and a cadence of 45 s. The AIA channels were first co-aligned with each other and interpolated to the SST plate scale. Cross correlation between the nearly simultaneous AIA 1700 Å and photospheric wing images was then used to establish coordinated alignment with SST observations.

Appendix B
Estimation of Multi-height Doppler Velocities Using the Ca II 8542 Å Spectral Line

The Doppler velocities were estimated at three spectral positions of the Ca II 8542 Å line corresponding to different formation heights in the chromosphere. These positions are located at $\Delta\lambda = -0.3$ Å, $\Delta\lambda = -0.15$ Å, and the line center, representing progressively higher layers of the chromosphere. The selected wavelength positions and the procedure used to estimate the velocities are illustrated on the normalized average quiet-Sun Ca II 8542 Å spectral profile shown in Figure 8.

[11] https://dubshen.astro.su.se/sst_archive/search

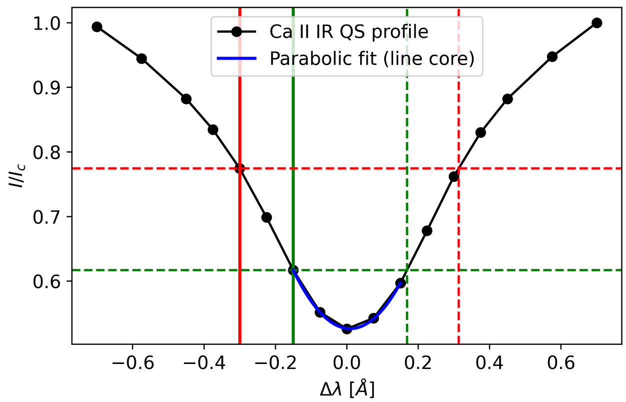

Figure 8. The black curve represents the normalized average quiet-Sun Ca II 8542 Å. The solid red and green vertical lines indicate the selected wavelength positions in the blue wing ($\Delta\lambda = -0.3$ Å and $\Delta\lambda = -0.15$ Å) used for the bisector velocity estimation. The dashed horizontal lines mark the corresponding intensity levels, while the dashed vertical lines indicate the interpolated wavelengths in the red wing having the same intensity. The midpoint between the blue and red wavelengths provides the Doppler shift used to estimate the bisector velocities. The blue curve shows the parabolic fit applied around the line core to determine the line center Doppler velocity.

For the wing positions (−0.3 and −0.15 Å), Doppler velocities were derived using the bisector method. For a given wavelength position in the blue wing, the corresponding intensity level was first determined from the spectral profile. The wavelength in the red wing having the same intensity was then obtained through interpolation of the spectral profile. The Doppler shift was estimated from the midpoint between the blue and red wavelengths,

For the wing positions (−0.3 and −0.15 Å), Doppler velocities were derived using the bisector method. This approach has been previously employed in earlier work by R. Chaurasiya & A. R. Bayanna (2025), where the bisector velocities were also compared with other velocity estimation techniques to ensure the robustness of the derived Doppler shifts. In the bisector method, for a given wavelength position in the blue wing, the corresponding intensity level is first determined from the spectral profile. The wavelength in the red wing having the same intensity is then obtained through interpolation of the spectral profile. The Doppler shift is estimated from the midpoint between the blue and red wavelengths.

$$\Delta\lambda = \frac{\lambda_b + \lambda_r}{2} - \lambda_{\rm ref},$$

where λ_b and λ_r represent the wavelengths in the blue and red wings with identical intensities. The corresponding Doppler velocity was then calculated using

$$v = \frac{\Delta\lambda}{\lambda_{\rm ref}} \times c,$$

where c is the speed of light and $\lambda_{\rm ref}$ is the reference wavelength.

For the line center velocity, a parabolic function was fitted to the spectral points around the minimum of the Ca II 8542 Å line profile. The wavelength corresponding to the minimum of the fitted parabola was taken as the observed line center position. The shift of this minimum relative to the reference wavelength provides the Doppler shift, which was then converted to velocity using the same relation given above.

The reference wavelength $\lambda_{\rm ref}$ was determined from the average Ca II 8542 Å profile computed over a quiet-Sun region within the field of view.

Appendix C
Mass Flux Carried Upward by the PCDs

To estimate the mass flux transported upward by the observed PCDs, we performed a differential emission measure (DEM; M. C. M. Cheung et al. 2015; Y. Su et al. 2018) analysis using the optically thin AIA EUV channels. The DEM, in units of cm^{-5} K^{-1}, is defined as

$$\mathrm{DEM}(T) = \int n_e^2(T)\, ds, \tag{C1}$$

where $n_e(T)$ is the electron number density of plasma at temperature T and s is the line-of-sight coordinate. We integrated the DEM over the temperature range of $\log T = 5.7$–6.1 to obtain the emission measure,

$$\mathrm{EM} = \int_{T_1}^{T_2} \mathrm{DEM}(T)\, dT. \tag{C2}$$

Assuming that the emitting plasma is approximately uniform along the line of sight, the electron number density was estimated as

$$n_e = \sqrt{\frac{\mathrm{EM}}{s}}, \tag{C3}$$

where the effective line-of-sight depth s was taken to be 3 AIA pixels, corresponding to the typical width of the observed coronal loop. The mass density of the coronal plasma was calculated assuming a fully ionized hydrogen helium plasma with a helium-to-hydrogen number density ratio of $\alpha = n_{\rm He}/n_{\rm H} \approx 0.1$ (M. Asplund et al. 2009; G. Del Zanna 2025). Under this assumption, the mass density can be written as

$$\rho \approx 1.2\, m_p\, n_e, \tag{C4}$$

where m_p is the proton mass.

Finally, the mass flux associated with the PCDs was estimated as

$$F_m = \rho\, v, \tag{C5}$$

where v is the projected plane-of-sky velocity of the PCDs measured from the AIA 171 Å observations. The estimated mass flux values are 9.06×10^{-9}, 6.69×10^{-9}, and 1.1×10^{-8} g cm^{-2} s^{-1} for the three cases shown in Figure 3, yielding an average mass flux of $\sim 9 \times 10^{-9}$ g cm^{-2} s^{-1}.

Appendix D
Two Additional Examples of Shock-driven Spicules and the Associated PCDs

Two more examples of shock-driven spicules from observations, presented in the same format as in Figure 2, are shown in Figures 9 and 10, while the associated space–time maps illustrating the evolution of the spicules and related PCDs are shown in Figures 11 and 12.

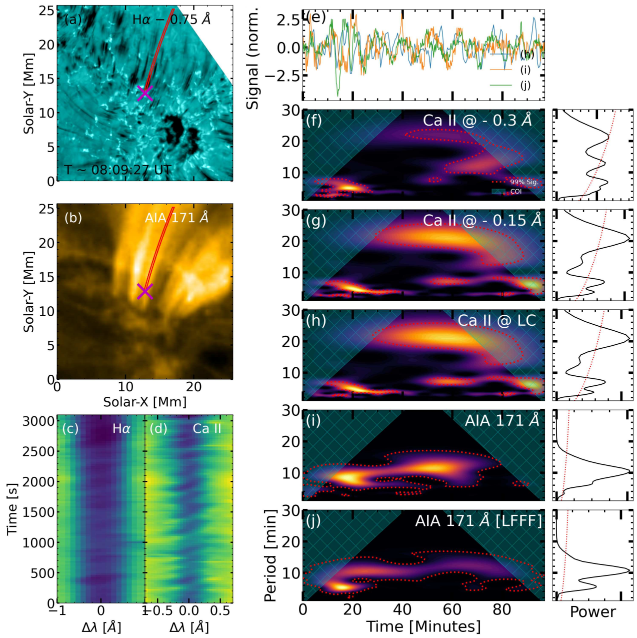

Figure 9. Similar to Figure 2 and also indicated by the green magnetic field line in Figure 13.

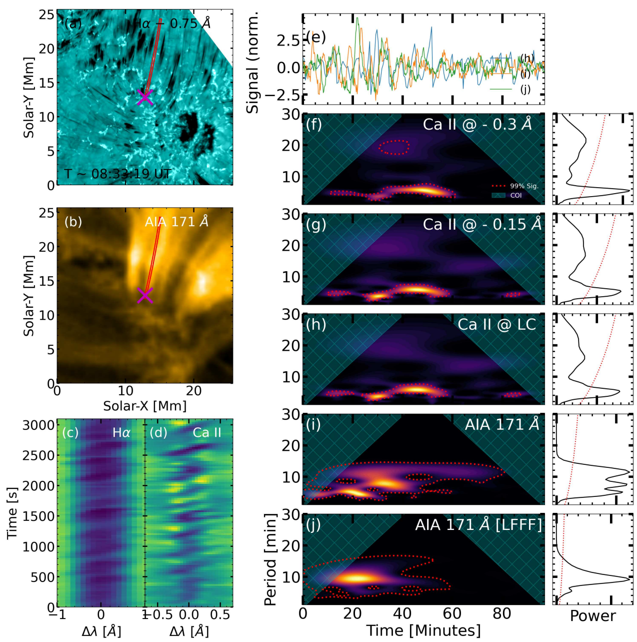

Figure 10. Similar to Figure 2 and also indicated by the blue magnetic field line in Figure 13.

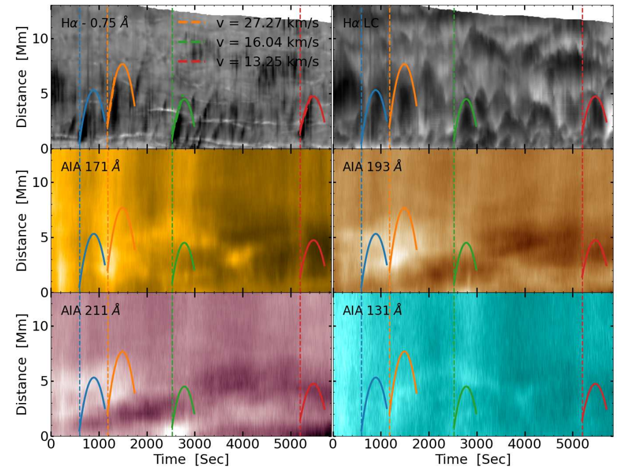

Figure 11. Same as Figure 3, but for the slit location shown in Figure 9.

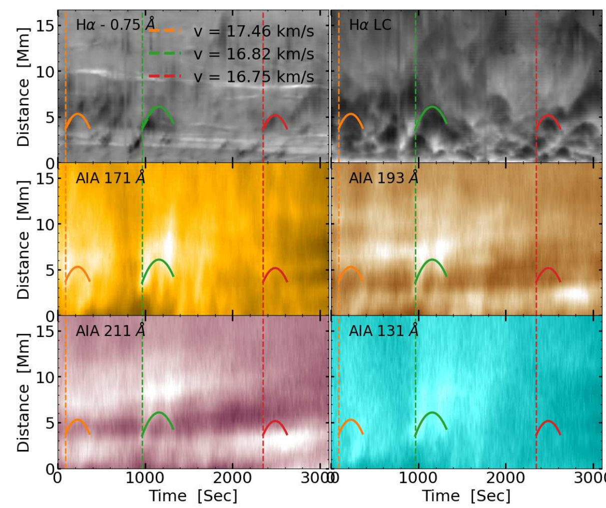

Figure 12. Same as Figure 3, but for the slit location shown in Figure 10.

Appendix E
Linear Force-free Magnetic Field Extrapolation

To investigate the three-dimensional magnetic field configuration and determine the magnetic field-aligned propagation location in the observations, we performed a LFFF extrapolation using the implementation available in the SolarSoftWare (SSWIDL) package.

The LFFF extrapolation assumes a force-free magnetic field condition,

$$\nabla \times \boldsymbol{B} = \alpha \boldsymbol{B}, \tag{E1}$$

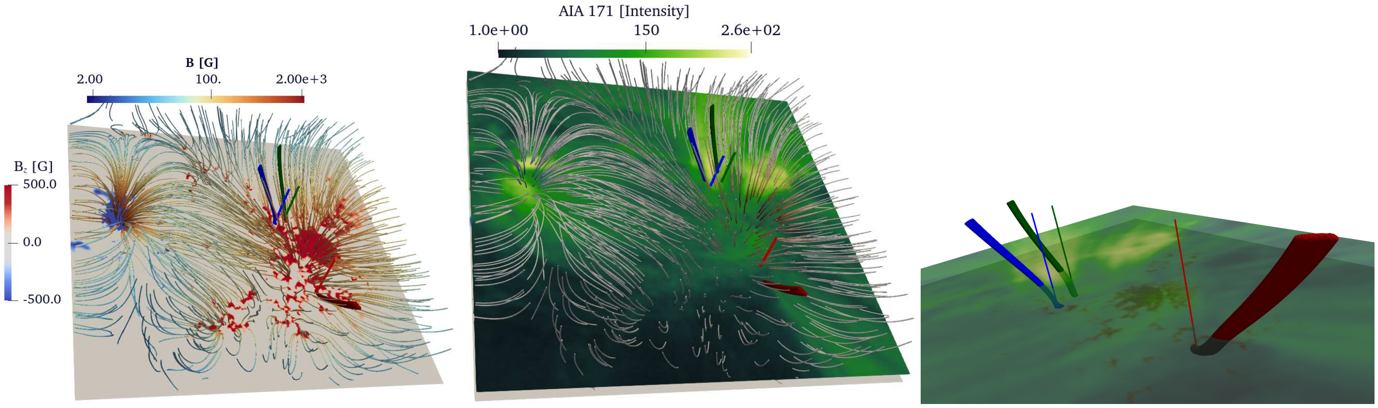

Figure 13. Three-dimensional magnetic field structure derived from the LFFF extrapolation, with the photospheric magnetic field displayed at the lower boundary. The three thick magnetic field lines shown in red, green, and blue correspond to the magnetic field orientations at the three shock locations illustrated in Figures 2, 9, and 10, respectively. The straight vertical lines represent the corresponding positions assuming purely vertical propagation. The left panel presents the full 3D magnetic field configuration together with the magnetic field strength $|\boldsymbol{B}|$, with the photospheric line-of-sight magnetic field shown at the base. The middle panel displays the AIA 171 Å intensity map overlaid on the same field configuration at a height of approximately 3 Mm above the photosphere. The right panel provides a zoomed-in view of the regions containing the analyzed shock wave locations.

where α is a constant force-free parameter that describes the twist of the magnetic field. This approximation is generally valid in the solar corona, where the plasma-β is low, and the magnetic pressure dominates over the plasma pressure.

As the lower boundary condition, we used the photospheric line-of-sight magnetic field ($B_{\rm LOS}$) obtained from the `PyMilne` inversion of the Fe I 6173 Å spectropolarimetric observations.

The SST magnetic field maps contained regions with missing values (NaNs) near the edges of the field of view. To obtain a continuous and physically consistent boundary condition, these NaN pixels were replaced with co-aligned HMI line-of-sight magnetograms. The HMI magnetograms were spatially co-registered and resampled to match the SST field of view and pixel scale. The resulting combined magnetic field map was then used as the lower boundary input for the LFFF extrapolation code. This extrapolation provides the three-dimensional magnetic field structure above the photosphere, allowing us to trace magnetic field lines originating from the regions of interest, as shown in Figure 13. The extrapolation was performed within a box of size $57 \times 57 \times 8.57$ Mm^3 along the X, Y, and Z directions, respectively.

These extrapolated magnetic field lines were subsequently used to determine the field-aligned trajectories along which the wavelet analysis of the AIA 171 Å intensity signal was performed. Specifically, the AIA 171 Å signal was taken at a height of approximately 3 Mm along the extrapolated magnetic field lines from the lower boundary, corresponding to the typical formation height of the lower coronal plasma observed in this channel. This approach enables us to investigate the propagation of the shock along the realistic magnetic field geometry, rather than assuming purely vertical propagation.

Appendix F
Automated Detection of Shocks in Simulations

We developed our own Python version of the IDL code by B. Snow et al. (2021)[12] for automated shock identification and classification in 2D MHD simulations. The code robustly identifies and classifies all the slow and fast shocks in a given 2D simulation. The first step is to identify the candidate shock locations as the ones where the velocity convergence $-\nabla \cdot \boldsymbol{u}$ exceeds a threshold value appropriate to the simulation run. The unit vectors normal and parallel to the shock at the candidate location are then calculated using the density gradient. The locations that do not correspond to the local maximum of the normal derivative of density are filtered out to avoid multiple detections due to finite shock width. By default, we consider 3 grid points on both sides of the shock candidate location along the normal direction for calculations. Next, the shock velocity v_s is estimated from mass conservation using the upstream (u) and downstream (d) values of density ρ and perpendicular flow velocity $u_\perp$ as $v_s = [(\rho^{\rm d} u_\perp^{\rm d} - \rho^{\rm u} u_\perp^{\rm u})/(\rho^{\rm u} - \rho^{\rm d})]$. Then, by using the perpendicular flow velocity transformed to the shock frame through v_s, the code calculates upstream and downstream Mach numbers for the perpendicular flow based on the characteristic linear wave speeds for slow and fast ideal MHD waves. If we find a transition in the corresponding Mach number from values >1 to <1 across the compression, the candidate is identified as a shock location. It can also be classified as a slow or a fast shock.

For both the simulation runs in this study, we take a threshold value of $5 \times 10^{-2}\,{\rm s}^{-1}$ for velocity convergence, which is reasonably low in order to identify all possible shock candidates. The strong flow convergence regions plotted in blue in panels (c) and (g) of Figure 6 are the regions where the convergence exceeds this threshold value. We note that the final shock identification is fairly independent of this initial threshold since it is based on Mach number calculations. We focus only on the detection of slow shocks in the simulations performed here.

Appendix G
Calculation of Synthetic Emission

The synthetic intensity was calculated using the formula

$$I_\lambda = \int G_\lambda(\rho, T)\rho^2 ds, \quad \text{(G1)}$$

while ignoring the line-of-sight integration (that is, along ds) for our 2D simulations. For the AIA 171 Å emission, we used the corresponding temperature response function for $G_\lambda(\rho, T)$. The expression for $G_\lambda(\rho, T)$ for the 15,000 K emission, along with more details, can be found in S. Srivastava et al. (2025).

[12] The IDL code is publicly available at https://github.com/AstroSnow/Orszag-Tang-Shock-Detection.

ORCID iDs

Ravi Chaurasiya https://orcid.org/0009-0002-0549-1446
Sankalp Srivastava https://orcid.org/0009-0000-2614-254X
Piyali Chatterjee https://orcid.org/0000-0002-0181-2495
Sahel Dey https://orcid.org/0000-0002-3369-8471
Robertus Erdélyi https://orcid.org/0000-0003-3439-4127
Ankala Raja Bayanna https://orcid.org/0000-0001-5802-7677

References

Asplund, M., Grevesse, N., Sauval, A. J., & Scott, P. 2009, ARA&A, 47, 481
Banerjee, D., Krishna Prasad, S., Pant, V., et al. 2021, SSRv, 217, 76
Beckers, J. M. 1972, ARA&A, 10, 73
Bose, S., Joshi, J., Testa, P., & De Pontieu, B. 2025, ApJL, 983, L7
Bryans, P., McIntosh, S. W., De Moortel, I., & De Pontieu, B. 2016, ApJL, 829, L18
Carlsson, M., De Pontieu, B., & Hansteen, V. H. 2019, ARA&A, 57, 189
Carlsson, M., & Stein, R. F. 1997, ApJ, 481, 500
Chae, J., Song, D., Seo, M., et al. 2015, ApJL, 805, L21
Chaurasiya, R., & Bayanna, A. R. 2025, MNRAS, 537, 2243
Chaurasiya, R., Bayanna, A. R., & Erdélyi, R. 2025, MNRAS, 543, 3791
Chaurasiya, R., Bayanna, A. R., Louis, R. E., Pereira, T. M. D., & Mathew, S. K. 2024, ApJ, 970, 179
Cheung, M. C. M., Boerner, P., Schrijver, C. J., et al. 2015, ApJ, 807, 143
de la Cruz Rodríguez, J. 2019, A&A, 631, A153
de la Cruz Rodríguez, J., Löfdahl, M. G., Sütterlin, P., Hillberg, T., & Rouppe van der Voort, L. 2015, A&A, 573, A40
De Pontieu, B., Erdélyi, R., & James, S. P. 2004, Natur, 430, 536
Del Zanna, G. 2025, MNRAS, 543, 390
Dey, S., Chatterjee, P. O. V. S. N., Murthyand Korsós, M. B., et al. 2022, NatPh, 18, 595
Ding, J. Y., Madjarska, M. S., Doyle, J. G., et al. 2011, A&A, 535, A95
González-Avilés, J. J., Guzmán, F. S., Fedun, V., & Verth, G. 2020, ApJ, 897, 153
Gopalan Priya, T., Su, J.-T., Chen, J., Deng, Y.-Y., & Prasad Choudhury, D. 2018, RAA, 18, 017
Hansteen, V. H., De Pontieu, B., Rouppe van der Voort, L., van Noort, M., & Carlsson, M. 2006, ApJL, 647, L73
Harris, C. R., Millman, K. J., van der Walt, S. J., et al. 2020, Natur, 585, 357
Heggland, L., Hansteen, V. H., De Pontieu, B., & Carlsson, M. 2011, ApJ, 743, 142
Hollweg, J. V. 1982, ApJ, 257, 345
Hunter, J. D. 2007, CSE, 9, 90
Iijima, H., & Yokoyama, T. 2017, ApJ, 848, 38
Jafarzadeh, S., Jess, D. B., Stangalini, M., et al. 2025, Nat. Rev. Methods Primers, 5, 21
Jiao, F., Xia, L., Li, B., et al. 2015, ApJL, 809, L17
Kesri, K., Dey, S., Chatterjee, P., & Erdelyi, R. 2024, ApJ, 973, 49
Lemen, J. R., Title, A. M., Akin, D. J., et al. 2012, SoPh, 275, 17
Liu, J., Nelson, C. J., Snow, B., Wang, Y., & Erdélyi, R. 2019, NatCo, 10, 3504
Löfdahl, M. G., Hillberg, T., de la Cruz Rodríguez, J., et al. 2021, A&A, 653, A68
Martínez-Sykora, J., De Pontieu, B., De Moortel, I., Hansteen, V. H., & Carlsson, M. 2018, ApJ, 860, 116
Martínez-Sykora, J., De Pontieu, B., Hansteen, V. H., et al. 2017, Sci, 356, 1269
Murawski, K., & Zaqarashvili, T. V. 2010, A&A, 519, A8
Ni, L., Lin, J., Samanta, T., et al. 2026, ApJL, 1000, L24
Noraz, Q., Carlsson, M., & Aulanier, G. 2026, A&A, 705, A86
Oxley, W., Scalisi, J., Ruderman, M. S., & Erdélyi, R. 2020, ApJ, 905, 168
Pencil Code Collaboration, Brandenburg, A., Johansen, A., et al. 2021, JOSS, 6, 2807
Pereira, T. M. D., De Pontieu, B., Carlsson, M., et al. 2014, ApJL, 792, L15
Pesnell, W. D., Thompson, B. J., & Chamberlin, P. C. 2012, SoPh, 275, 3
Roberts, B. 1979, SoPh, 61, 23
Rouppe van der Voort, L., De Pontieu, B., Pereira, T. M. D., Carlsson, M., & Hansteen, V. 2015, ApJL, 799, L3
Rouppe van der Voort, L. H. M., Rutten, R. J., Sütterlin, P., Sloover, P. J., & Krijger, J. M. 2003, A&A, 403, 277
Sakaue, T., & Shibata, K. 2020, ApJ, 900, 120
Samanta, T., Tian, H., Yurchyshyn, V., et al. 2019, Sci, 366, 890
Sand, M. O., Rouppe van der Voort, L. H. M., Joshi, J., et al. 2025, A&A, 697, A180
Scharmer, G. B., Bjelksjo, K., Korhonen, T. K., Lindberg, B., & Petterson, B. 2003, SPIE, 4853, 341
Scharmer, G. B., Narayan, G., Hillberg, T., et al. 2008, ApJ, 689, L69
Scherrer, P. H., Schou, J., Bush, R. I., et al. 2012, SoPh, 275, 207
Skirvin, S. J., Samanta, T., & Van Doorsselaere, T. 2024, A&A, 689, A135
Snow, B., Hillier, A., Murtas, G., & Botha, G. J. J. 2021, ExpR, 2, e35
Sow Mondal, S., Klimchuk, J. A., & Sarkar, A. 2022, ApJ, 937, 71
Srivastava, A. K., Singh, A., Singh, B., et al. 2024, RSPTA, 382, 20230220
Srivastava, S., Chatterjee, P., Dey, S., & Erdélyi, R. 2025, ApJ, 989, 39
Su, Y., Veronig, A. M., Hannah, I. G., et al. 2018, ApJL, 856, L17
Suematsu, Y., Wang, H., & Zirin, H. 1995, ApJ, 450, 411
The SunPy Community, Barnes, W. T., Bobra, M. G., et al. 2020, ApJ, 890, 68
Tsiropoula, G., Alissandrakis, C. E., & Schmieder, B. 1994, A&A, 290, 285
Tsiropoula, G., Tziotziou, K., Kontogiannis, I., et al. 2012, SSRv, 169, 181
Van Noort, M., Rouppe Van Der Voort, L., & Löfdahl, M. G. 2005, SoPh, 228, 191
Virtanen, P., Gommers, R., Oliphant, T. E., et al. 2020, NatMe, 17, 261
Withbroe, G. L., & Noyes, R. W. 1977, ARA&A, 15, 363
Yurchyshyn, V., Abramenko, V., & Goode, P. 2013, ApJ, 767, 17